



Microstructure, mechanical and corrosion performance of magnetron sputtered $(\text{Al}_{0.5}\text{CoCrFeNi})\text{N}_x$ high-entropy alloy nitride films

Fanyong Zhang^{a,*}, Honglu Ma^a, Ruibin Zhao^a, Guangxing Yu^a, Jiawen Chen^a, Fuxing Yin^{a,b}

^a Tianjin Key Laboratory of Materials Laminating Fabrication and Interface Control Technology, School of Material Science and Engineering, Hebei University of Technology, Tianjin 300130, China

^b Institute of New Materials, Guangdong Academy of Sciences, Guangzhou 510650, China



ARTICLE INFO

Keywords:

High-entropy alloy
Nitride films
Magnetron sputtering
Microstructure
Corrosion properties

ABSTRACT

High-entropy alloy nitride (HEAN) films of $(\text{Al}_{0.5}\text{CoCrFeNi})\text{N}_x$ were deposited on 304 steel and silicon plates using reactive DC magnetron sputtering. The effect of nitrogen flow fraction ($R_N = 0\%, 6\%, 13\%, 23\%, 40\%$) on the microstructure and performance of HEAN films was studied. The deposition rate showed a negative relationship with the nitrogen flow ratio. The N concentration raised with the increasing R_N ratio, reaching a maximum value of 33 at% ($R_N = 40\%$). The as-deposited $\text{Al}_{0.5}\text{CoCrFeNi}$ film presented an FCC + BCC dual phase structure. With the addition of nitrogen, the HEAN film transformed FCC + BCC structure to a composite structure composed of FCC nanocrystals and amorphous. All the HEAN films grew the smooth surface with nano-clusters. With increasing R_N ratio, the average size of clusters decreased from 203 nm to 83 nm, resulting in a denser film. The HEAN films exhibited enhanced hardness, retaining relatively good plasticity. The hardness and elastic modulus reached a maximum value of 14.42 GPa and 212 GPa at $R_N = 23\%$, respectively. The HEAN films showed good adhesion with substrate and had no obvious cracks during scratching. Under 3.5 wt% NaCl solution, the increasing R_N ratio contributed to the higher E_{corr} and lower i_{corr} for HEAN films, with excellent corrosion resistance ($E_{corr} = 0.054$ V, $i_{corr} = 0.72 \mu\text{A}/\text{cm}^2$) at $R_N = 23\%$. The incorporation of N showed promising potential in improving the performance of AlCoCrFeNi alloy.

1. Introduction

High-entropy alloys (HEAs) are composed of at least five primary elements, with individual concentrations typically ranging from 5 to 35 at%, which prefer to generate simple solid-solutions (FCC, BCC, HCP, etc.) instead of complex or intermetallic compound [1–3]. Four core effects are known for HEAs including high mixing entropy, slow diffusion, large lattice distortion and cocktail effect [4,5]. Due to the distinct structure, HEA exhibit excellent properties such as favorable mechanical properties, high-temperature stability, oxidation and corrosion resistance, etc [6,7]. HEA films possess exceptional bulk properties, which render them highly promising for use as protective materials [8–10]. Small-radius elements like C, B, and N are possible to occupy interstices in the lattice of HEAs, forming interstitial solid solutions and regulating the properties of HEAs. In recent years, the investigation of high-entropy alloy nitride (HEAN) films has attracted extensive attention owing to their superior mechanical characteristics and resistance to corrosion

[11–13].

The AlCoCrFeNi -based HEA is among the most extensively studied HEA systems. Wang et al. [14] were able to significantly enhance the hardness of AlCoCrFeNi HEA from 522 to 720 HV through plasma nitriding, resulting in superior wear resistance compared to the cast alloy. Compared with plasma nitriding, reactive magnetron sputtering has the obvious advantage of allowing for the adjustment of film properties through the control of reaction gases (such as O_2 and N_2), as well as the ability to fine-tune the deposition parameters to regulate the microscopic morphology of the films [12,13]. Additionally, it is widely used due to its uniform film formation, low substrate temperature to minimize temperature effects, and environmental safety [15].

As reported, reactive magnetron sputtering has been utilized to prepare a series of HEAN films which can be subdivided into non-strong nitride forming elements HEAN (like CoCrFeMnNi [16]) and strong nitride forming elements HEAN (like AlCrTiZrV [17]). Khan et al. [18] deposited $\text{AlCoCrCu}_{0.5}\text{FeNi}$ HEAN films by varying nitrogen flow

* Correspondence to: School of Material Science and Engineering, Hebei University of Technology, No. 8 Guangrong Road, Hongqiao District, Tianjin 300130, China.

E-mail address: fany_zhang@163.com (F. Zhang).

Table 1
Deposition parameters of $(\text{Al}_{0.5}\text{CoCrFeNi})\text{N}_x$ films.

R_N (%)	Target power (W)	Gas flow (sccm)	
		Ar	N_2
0	150	50	0
6	150	50	3.2
13	150	50	7.5
23	150	50	15
40	150	50	33

fractions. The increased nitrogen flow produced interstitial nitrogen atoms, reducing film crystallinity and creating an amorphous phase, and the films achieved high hardness (9.8 GPa) and elastic modulus (149 GPa). Garah et al. [19] fabricated amorphous single-phase (AlTiZrTaHf) N HEAN films with a non-columnar dense structure, reaching maximal hardness and modulus (27.67 GPa and 205.56 GPa), significantly higher than AlTiZrTaHf . Zhang et al. [20] found that the $(\text{CrNbTiAlV})\text{N}$ films showed greatly enhanced hardness (> 40 GPa) and open circuit potential (~ -0.1 V) than the CrNbTiAlV film. The studies by Chen et al. [21] and Si et al. [22] explore the impact of nitrogen introduction on the corrosion resistance of HEA films. Nitrogen changes the phase structure and growth pattern, resulting in a denser coating and improved corrosion resistance in 3.5 wt% NaCl solution. The value of charge transfer resistance for the coating gradually increases with increasing nitrogen content, and the current density decreases rapidly with increasing potential. In a word, the addition of N could significantly improve the mechanical and corrosion resistance of HEA films.

To date, there have been extensive studies on bulk properties of AlCoCrFeNi -based HEAs [23–25]. However, the effect of nonmetallic elements on AlCoCrFeNi alloys is still unclear. Therefore, it is necessary to reveal the microstructure and performance of AlCoCrFeNi alloys with the incorporation of nonmetallic elements (especially N), with the aim to explore its potential application. Magnetron sputtering can be conveniently used to introduce N into metal alloys by reaction with ionization atoms of N_2 . Thus, in this study, $\text{Al}_{0.5}\text{CoCrFeNi}$ target was employed to deposit HEAN films under Ar-N₂ condition through reactive magnetron sputtering. The nitrogen flow fractions ($R_N = \text{N}_2/(\text{Ar} + \text{N}_2)$) were adjusted to fabricate $(\text{Al}_{0.5}\text{CoCrFeNi})\text{N}_x$ films. The phase composition, growth morphologies, mechanical and corrosion performance of the films were investigated. It would provide guide for tailoring properties of AlCoCrFeNi -based HEAs.

2. Experimental details

2.1. Film deposition

High-entropy alloy nitride films (HEANFs) were deposited on 304

steel and silicon substrates at different nitrogen flow (R_N) using a magnetron sputtering system (JCP-500, Beijing Technol Science Co., Ltd.). A circular target of $\text{Al}_{0.5}\text{CoCrFeNi}$ ($\phi 50$ mm × 5 mm) fabricated by vacuum arc melting was utilized for depositing. The steel substrates were polished to a mirror finish prior to deposition, and then they underwent a 15 min ultrasonic cleaning procedure in ethanol. After drying, the substrates were placed onto a rotating holder inside the sputtering system.

High-purity Ar and N_2 were utilized during sputtering process. The chamber was pumped to a base pressure of 4.0×10^{-3} Pa. Pre-sputtering was conducted to clean substrates for 15 min under Ar conditions (4.1 Pa) at a bias of -920 V. The target surface was also sputtering-cleaned for 5 min under Ar pressure (0.56 Pa). Then, N_2 was introduced for reactive sputtering. As seen from Table 1, the flows of Ar and N_2 were adjusted to achieve different R_N of 0%, 6%, 13%, 23%, and 40%. The working pressure was 0.56 Pa. The power of $\text{Al}_{0.5}\text{CoCrFeNi}$ target was 150 W. The sample holder rotated at 10 rpm and maintained a bias voltage of -80 V throughout the deposition for 2 h.

2.2. Characterization

The phase structure of all the films was analyzed using a Bruker D8 Advance X-ray diffractometer. Cu-K α radiation was employed, and the analysis was performed in the grazing angle diffraction mode. The scanning range is 20° – 100° , and the grazing angle is 1° . The

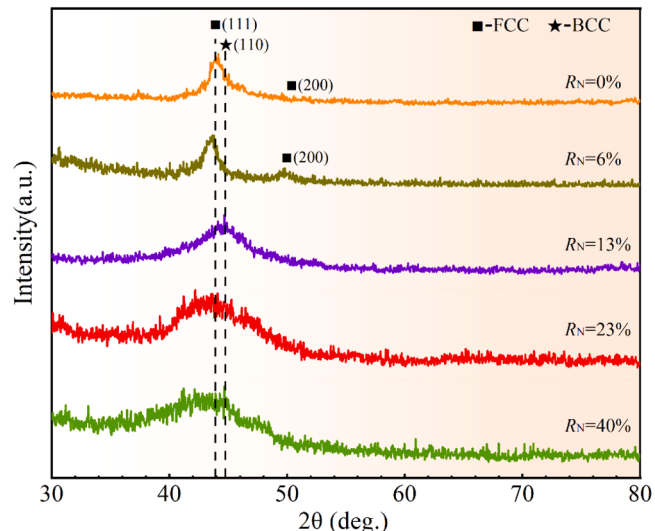


Fig. 2. XRD patterns of $(\text{Al}_{0.5}\text{CoCrFeNi})\text{N}_x$ films deposited at different R_N .

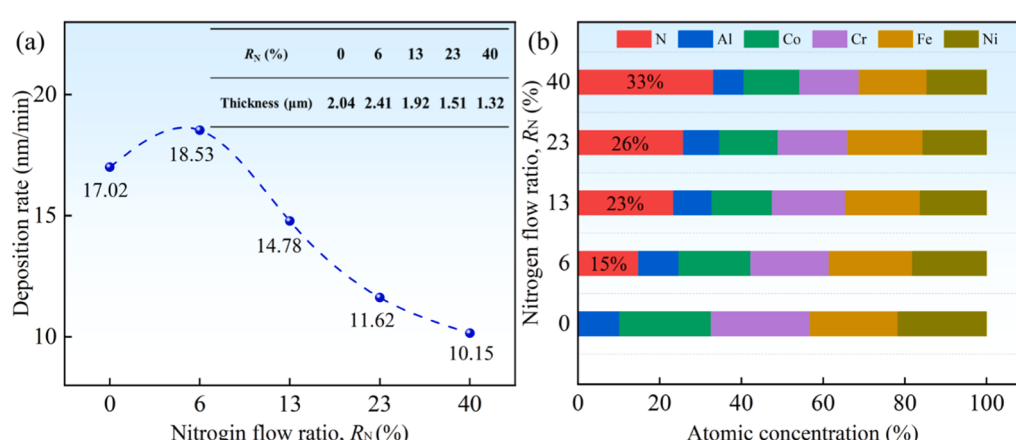


Fig. 1. Deposition rate (a) and surface composition (b) of $(\text{Al}_{0.5}\text{CoCrFeNi})\text{N}_x$ films deposited at different R_N .

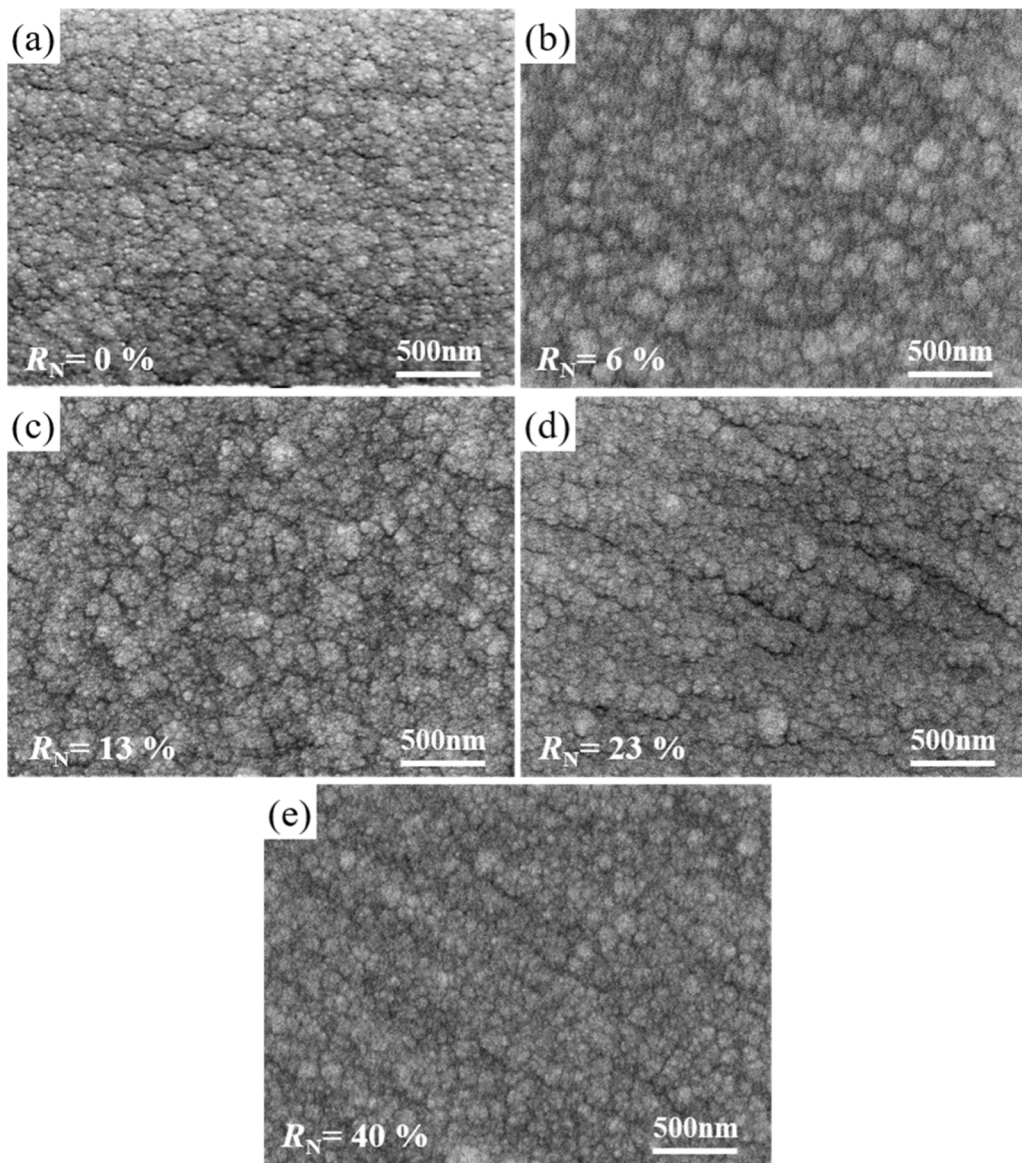


Fig. 3. Surface morphology of $(\text{Al}_{0.5}\text{CoCrFeNi})\text{N}_x$ films deposited at different R_{N} : (a) $R_{\text{N}} = 0\%$, (b) $R_{\text{N}} = 6\%$, (c) $R_{\text{N}} = 13\%$, (d) $R_{\text{N}} = 23\%$, (e) $R_{\text{N}} = 40\%$.

morphology and chemical composition of the films were examined through the utilization of a JSM7100F scanning electron microscope (SEM), which was outfitted with an energy dispersive X-ray spectrometer (EDS, EDAX Genesis 2000). Using an electron probe micro analyzer (EPMA, JXA-8530, JEOL), the distribution of surface elements in HEANFs was examined. The detailed microstructure of films was observed by means of a transmission electron microscope (TEM, TECNAI G2, 200 kV).

Using an Anton Paar nano-indenter, the surface hardness and elastic modulus of HEAN films were measured. A micro-hardness tester (HMV-G, Shimadzu, Japan) was used to measure the fracture toughness of the films under a 0.98 N stress. Scratch tests were conducted using a diamond tip on a micro-scratch tester (WS-2005, Lanzhou Institute of Chemical Physics) to evaluate the fracture resistance and adhesive strength of films. During the test, a load of 80 N was applied at its maximum, with a loading rate of 80 N/min. The scratch encompassed a 3 mm area.

The corrosion characteristics of HEANFs in a 3.5 wt% NaCl solution were investigated using an electrochemical workstation (CHI660E). For the test, a three-electrode system was utilized, comprising a standard calomel electrode, a counter electrode made of platinum (Pt), and a

working electrode consisting of HEAN films. A stable circuit potential was achieved by soaking the electrodes into the solution for 1 h. The scan rate used for the polarization test was 0.1 mV/s. Electrochemical impedance spectroscopy (EIS) tests were conducted using a 10 mV AC amplitude and a frequency range of $10^{-2} \sim 10^5$ Hz. The polarization test was conducted at 0.1 mV/s scan rate. Tests of electrochemical impedance spectroscopy (EIS) were performed with the 10 mV AC amplitude and the $10^{-2} \sim 10^5$ Hz frequency range. After the polarization test, the corrosion morphology was examined using SEM.

3. Results and discussions

3.1. Deposition rate and surface composition of HEAN films

The deposition rate and surface composition of HEAN films are shown in Fig. 1. As seen from Fig. 1a, at $R_{\text{N}} = 0\%$, the films were deposited at a rate of 17.02 nm/min. As N_2 was introduced, the deposition rate of the films first increases to 18.53 nm/min at $R_{\text{N}} = 6\%$, then decreases with further increasing R_{N} . Note that the deposition rate falls sharply to 10.15 nm/min at $R_{\text{N}} = 40\%$. Such could be due to poisoning of the target and lower sputtering efficiency of N_2 as reactive gas ions than

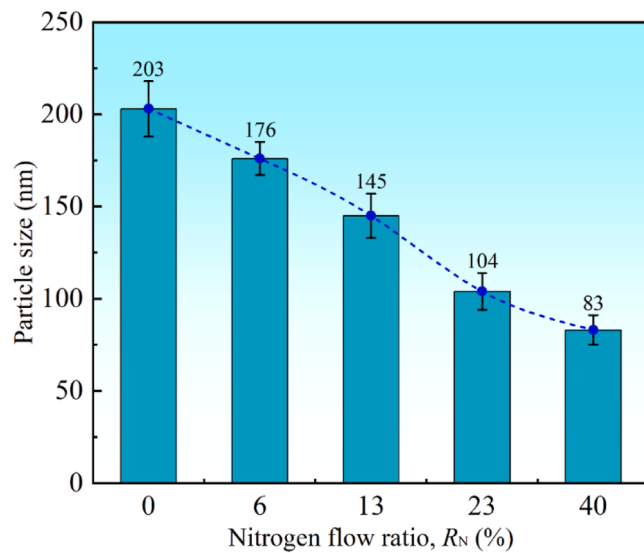


Fig. 4. Particle size of $(\text{Al}_{0.5}\text{CoCrFeNi})\text{N}_x$ films deposited at different R_N .

that of Ar [26,27]. As seen from the inset table, the thickness of $(\text{Al}_{0.5}\text{CoCrFeNi})\text{N}_x$ at $R_N = 6\%$ is $2.41 \mu\text{m}$, much larger than that of $\text{Al}_{0.5}\text{CoCrFeNi}$ film ($2.04 \mu\text{m}$). With increasing R_N ratio, the film thickness is less than $2 \mu\text{m}$. The surface chemical composition of as-deposited films measured by EDS are displayed in Fig. 1b. The films at $R_N = 0\%$ shows approximately equimolar ratio of Co, Cr, Ni and Fe, while Al has half the atomic content Cr. It implies the as-deposited HEA film could well retain the composition of the $\text{Al}_{0.5}\text{CoCrFeNi}$ target. As the R_N ratio increases from 0% to 40%, the metal content gradually decreases, whereas the N content increases to 33 at%. $\text{Al}_{0.5}\text{CoCrFeNi}$ is a non-strong nitride forming element HEA, as reported by Depla et al. [16], the highest N content in CoCrFeMnNi films reached about 30 at%. Similarly, Khan et al. [18] reported the highest N content of 10.6 at% in $\text{AlCoCrCu}_{0.5}\text{FeNi}$ HEAN films. However, in HEAN films with strong nitride-forming elements, the N content exceeds 40 at% and even reaching 50 at% [17,19,20].

3.2. Phase analysis of HEAN films

Fig. 2 displays the XRD patterns of $(\text{Al}_{0.5}\text{CoCrFeNi})\text{N}_x$ HEAN films at different R_N . In $\text{Al}_x\text{CoCrFeNi}$, Al is considered as a BCC stabilizer [28]. As the Al content increasing, there is a transition from the FCC to the BCC crystal structure. When $0.5 \leq x \leq 0.9$ [29], the alloy consists of a mixture of FCC and BCC phases. Similar to the bulk material, the films also exhibit a mixed FCC and BCC crystal structure. At $R_N = 0\%$, the $\text{Al}_{0.5}\text{CoCrFeNi}$ film shows broad peak ranging from $42^\circ - 47^\circ$, with strong peak of FCC structure at 43.9° (111) and weak peak of BCC structure at 44.7° (110). FCC (111) and BCC (110) peaks have similar crystal spacing around 44° and are present together in the broader diffraction peaks. With introducing N₂ at $R_N = 6\%$, the HEAN film retains the broad peaks with mixed phases of FCC and BCC, but the FCC peak shifts to the left. It implies the N dissolving into the FCC lattice, causing the lattice expansion. With further increasing R_N ($>13\%$), the FCC peak at 43.9° becomes significant broader and shifts to low angles more obviously. Meanwhile, the FCC peak at 50.6° (200) disappears, as well as the BCC peaks. Such indicates the higher N addition leads to the refinement of crystals and formation of amorphous structure. As reported by Khan et al. [18], the increase in R_N ratio also changed the crystalline structure of $\text{AlCoCrCu}_{0.5}\text{FeNi}$ film into partially amorphous. Furthermore, this conclusion was confirmed in former studies by Chen et al. [30] and Hsueh et al. [31].

3.3. Microstructures of HEAN films

Fig. 3 shows the surface morphology of HEAN films deposited at different R_N . All the films grow a smooth surface with cauliflower-like clusters. As for $\text{Al}_{0.5}\text{CoCrFeNi}$ film (Fig. 3a), the clusters are composed of larger globular particles. With the addition of N, lots of finer particles generate to form clusters and the surface becomes denser. Fig. 4 depicts the particle size of all the films. Notably, the $\text{Al}_{0.5}\text{CoCrFeNi}$ film (Fig. 3a) has an average particle size of $\sim 203 \text{ nm}$. The incorporation of N leads to the decrease of particle size with increasing R_N (6%, 13%, 23% and 40%), which are 176 nm, 145 nm, 104 nm, and 83 nm respectively. As displayed in XRD patterns, the flat and broaden peaks also indicate more obvious formation of nanocrystals at higher R_N (23% and 40%). EPMA was conducted to evaluate the homogeneity of films in Fig. 5. The as-deposited $\text{Al}_{0.5}\text{CoCrFeNi}$ film shows uniform distribution of constituent elements (Fig. 5a). Due to the different yield of Fe, Co, Cr and Ni under Ar-sputtering, tiny segregation (red spots) is visible in these

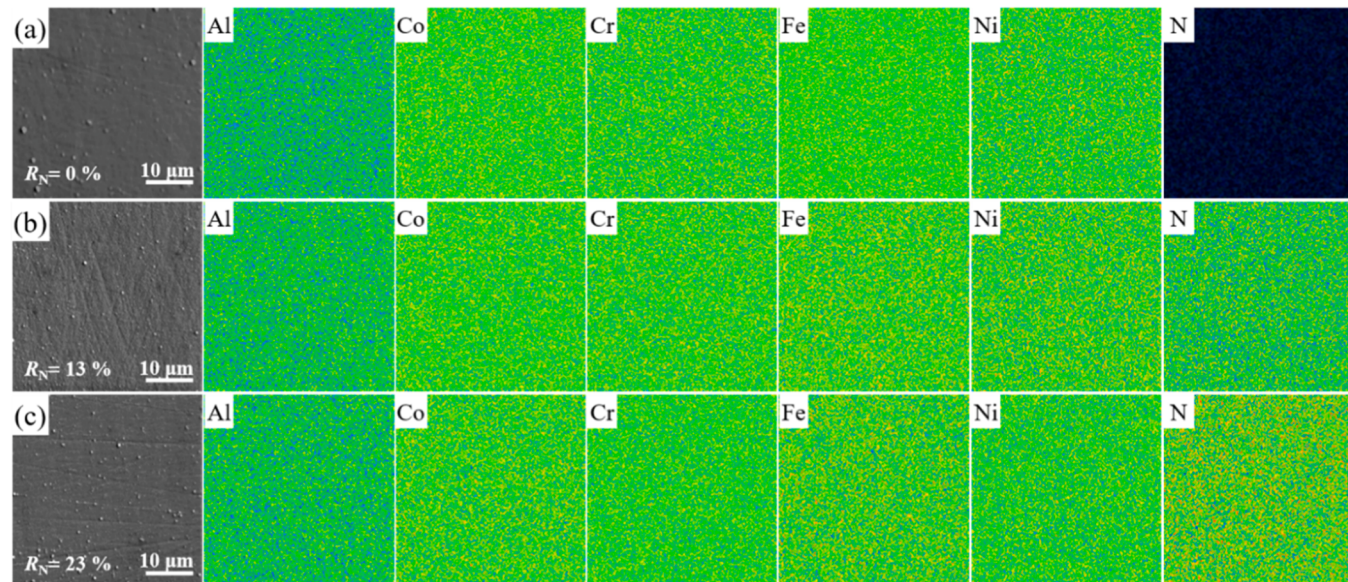


Fig. 5. Element distribution of $(\text{Al}_{0.5}\text{CoCrFeNi})\text{N}_x$ films deposited at different R_N : (a) $R_N = 0\%$, (b) $R_N = 13\%$, (c) $R_N = 23\%$.

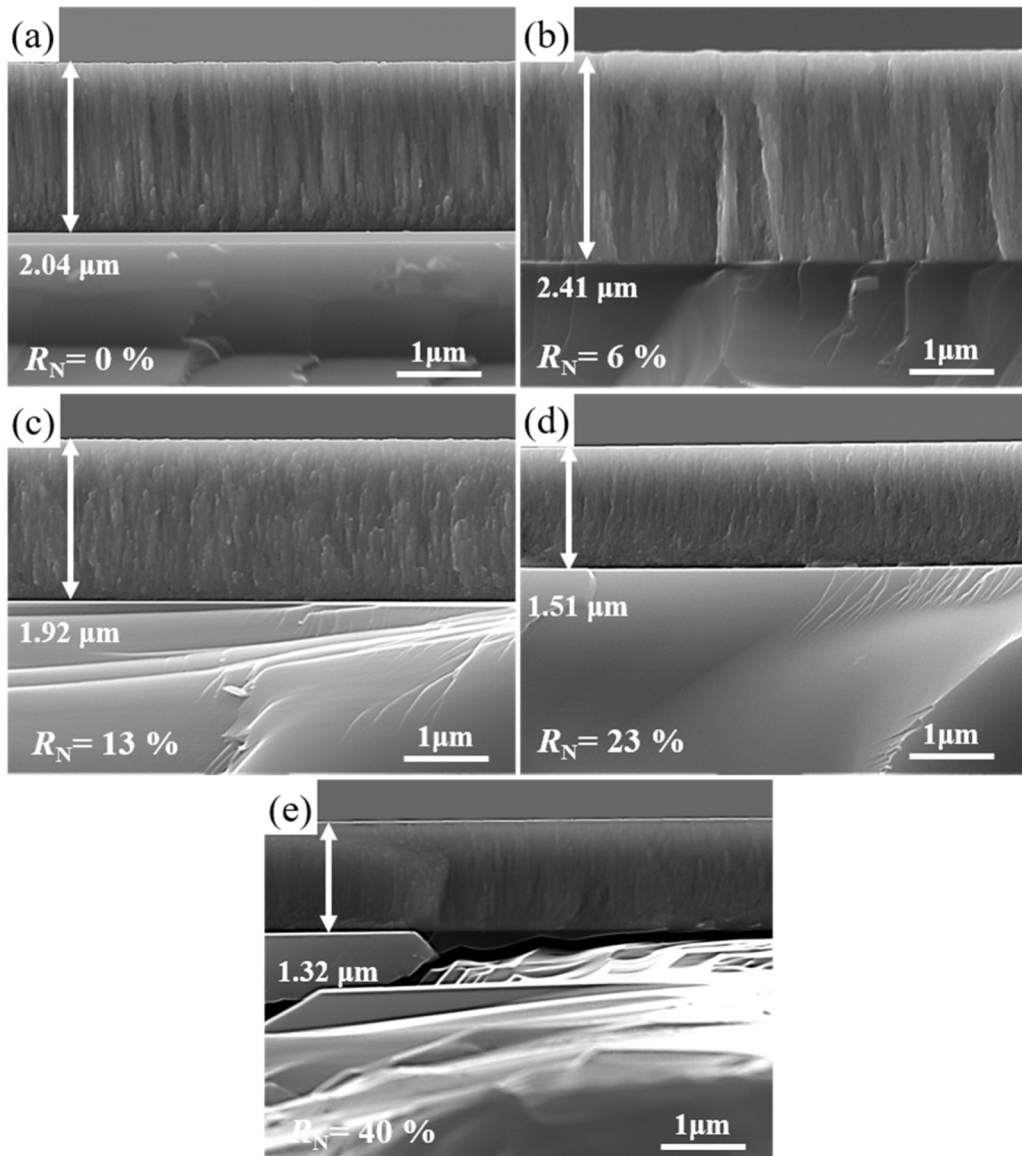


Fig. 6. Cross-sectional morphology of $(\text{Al}_{0.5}\text{CoCrFeNi})\text{N}_x$ films deposited at different R_N : (a) $R_N = 0\%$, (b) $R_N = 6\%$, (c) $R_N = 13\%$, (d) $R_N = 23\%$, (e) $R_N = 40\%$.

element maps. The HEAN films (Fig. 5b-c) maintain the uniform distribution of constituent elements. Note that the color of N maps change from blue (N-deficient) to green (N- incorporation). Moreover, the red color in the N map at high R_N ratio (23%) becomes more noticeable, indicating more N atoms introduced into the film.

Fig. 6 presents the cross-sectional SEM images of $(\text{Al}_{0.5}\text{CoCrFeNi})\text{N}_x$ films. All the films show a smooth fracture surface and uniform thickness with typical columnar structure. The $\text{Al}_{0.5}\text{CoCrFeNi}$ film grows a typical coarse columnar structure (Fig. 6a). As increasing R_N ratios, the columns become finer and denser (Fig. 6b-d). Note that the thickness of HEAN films decreases from $2.41 \mu\text{m}$ (6%) to $1.32 \mu\text{m}$ (40%). Actually, higher N_2 flow fraction promotes the combination between N atoms and HEA, but also results in the target poisoning, thus decreasing the depositing rate. During the process of sputtering, the N_2 flow simultaneously refines the columnar growth structure of the HEAN film and suppresses the sputtering rate of the HEA target material.

Fig. 7 shows the TEM images of the HEAN film deposited at $R_N = 23\%$. As seen from Fig. 7a, the microstructure exhibits mesh-like morphology with white boundary and internal gray areas. These white interfaces are ascribed to the columnar growth of films. The SAED pattern (Fig. 7b) indicates the amorphous characteristic of HEAN film.

Moreover, the HRTEM image (Fig. 7c) displays the magnified picture of the gray area in Fig. 7a, in which nanocrystal grains form in the amorphous matrix. The crystallite spacing of 0.211 nm and 0.207 nm (Fig. 7c) are determined as FCC phase. This co-existence feature is also supported by the inset FFT image (Fig. 7d), showing a typical halo ring mixed with discontinuous spots identified as FCC phase. Similar results are also observed in a deposited Cantor alloy film [32]. Furthermore, as seen from Fig. 7e-f, the nanocrystals are wrapped with glass shells and the crystal areas show irregular polygon shape with average size of 6 nm . These are consistent with the broad peaks in the XRD results. The increasing R_N ratio causes the shift of film structure from the crystalline phase to the amorphous structure.

The formation of amorphous phases in HEAs and their nitride films is typically affected by high mixing entropy and kinetic effects. The increased mutual solubility between the constituent elements, caused by the raised mixing entropy, prevents the formation of crystal structure [5, 8–10]. Furthermore, the rapid quenching during sputter deposition process effectively suppresses chemical composition fluctuation and crystallization [18]. Nitrogen could be considered as the sixth element in AlCoCrFeNi system, occupying interstitial spaces of lattice, thus introducing greater degree of chaos and disorder. Due to the large lattice

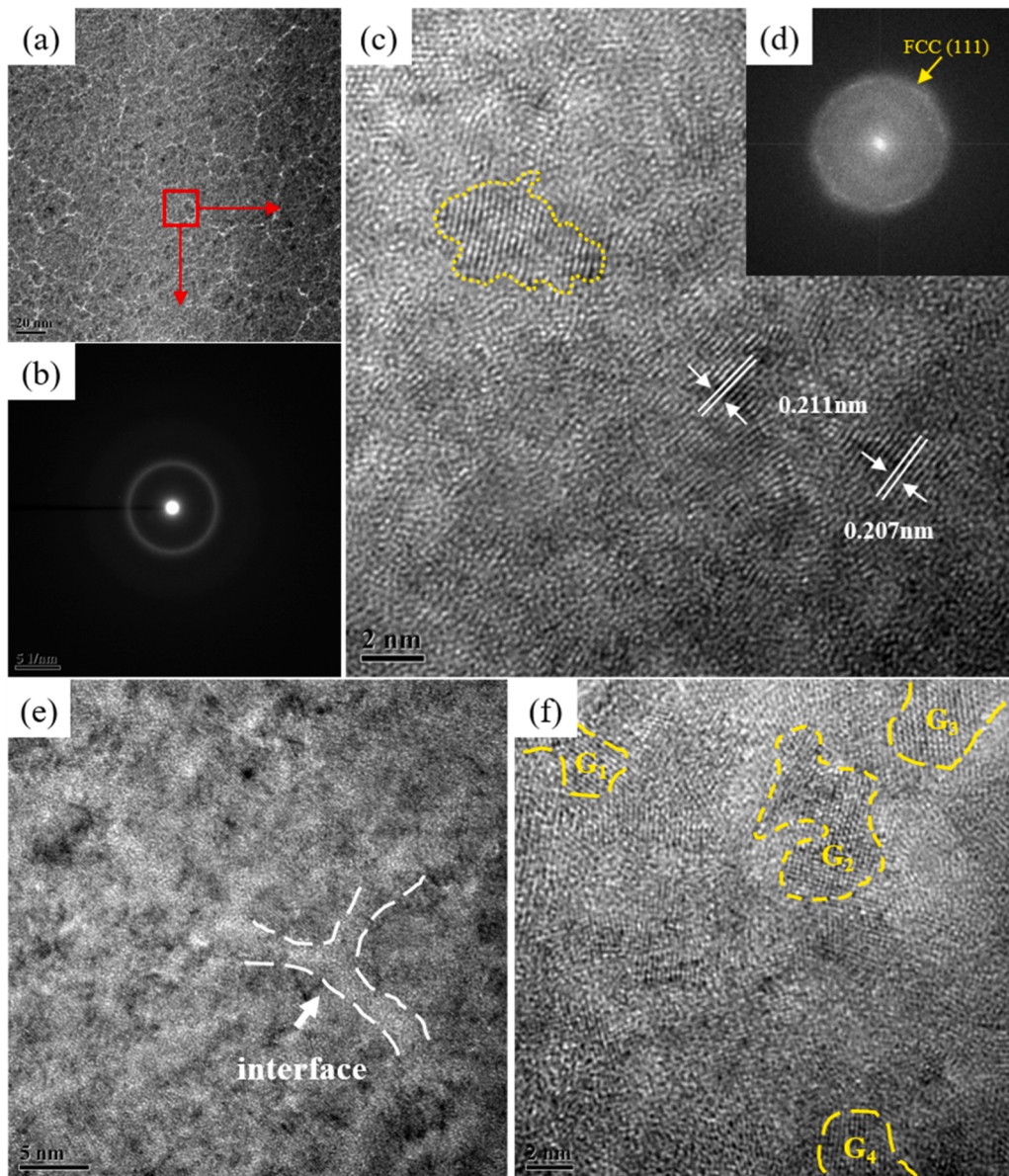


Fig. 7. TEM observation of $(\text{Al}_{0.5}\text{CoCrFeNi})\text{N}_x$ films deposited at $R_N = 23\%$: (a) bright field image, (b) selected area electron diffraction (SAED) patterns, (c, e and f) HRTEM image, (d) the FFT image of (c).

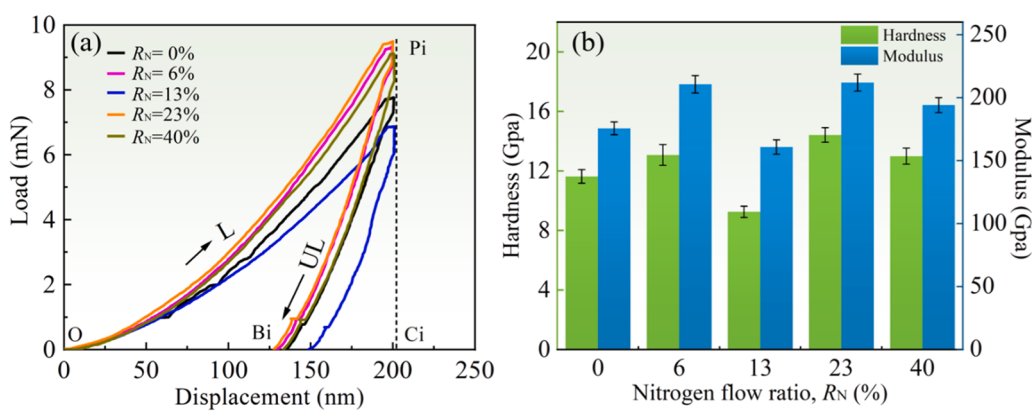


Fig. 8. Load-displacement curves (a) and hardness and elastic modulus (b) for nanoindentation results of $(\text{Al}_{0.5}\text{CoCrFeNi})\text{N}_x$ films deposited at different R_N .

Table 2
Calculated results from nano-indentation curves.

R_N (%)	H (GPa)	E (GPa)	W_p (nJ)	W_t (nJ)	η_p	H/E	H^3/E^2
0	11.63	175.7	0.373	0.592	0.63	0.066	0.051
6	13.07	210.6	0.426	0.688	0.62	0.062	0.050
13	9.25	160.8	0.401	0.529	0.76	0.058	0.031
23	14.42	212	0.453	0.729	0.62	0.068	0.067
40	12.99	194.1	0.438	0.671	0.65	0.067	0.058

parameter of the FCC phase, it can accommodate more nitrogen atoms. The excess N atoms in lattice interstitial can favor partial amorphization to reduce the Gibbs free energy of the whole structure, leading to partial transformation of FCC into amorphous phase. This is in agreement with previous study on HEAN films by Khan et al. [18]. As the R_N increases above 13%, more N atoms are incorporated in the film, thus the amorphous structure dominate in the film while the BCC phase tends to disappear.

From the XRD pattern (Fig. 2), the diffraction peaks gradually broaden as R_N increases, indicating a refinement in the crystal structure and the formation of an amorphous structure. The surface morphology (Fig. 3) reveals a smooth cauliflower-like cluster structure of HEAN

films. The cluster size (Fig. 4) gradually decreases (203 nm → 83 nm) with increasing R_N , indicating a more pronounced formation of nanocrystals, particularly at R_N of 23% and 40%. The cross-sectional images (Fig. 6) demonstrate that the HEAN films possess a uniform thickness and a longitudinal columnar structure. Moreover, an increase in R_N results in a finer and denser columnar structure. The TEM images (Fig. 7) provide insights into the microstructure of the HEAN films, showing both amorphous structure and nanocrystals. A higher nitrogen content ($R_N > 23\%$) leads to a greater proportion of amorphous structure and the formation of FCC nanocrystals. The above analysis shows that the introduction of nitrogen has a significant impact on the structure and properties of HEAN thin films, gradually transforming them from crystalline to amorphous structures. This transformation is influenced by high mixing entropy and kinetic effects.

3.4. Mechanical properties of HEAN films

Fig. 8 shows the nano-indentation test results of $(Al_{0.5}CoCrFeNi)N_x$ films. As seen from the load-displacement curves in Fig. 8a, at the same indentation depth (200 nm), the HEAN film reaches the highest load of 9.5 mN at $R_N = 23\%$, which is higher than that of $Al_{0.5}CoCrFeNi$ film

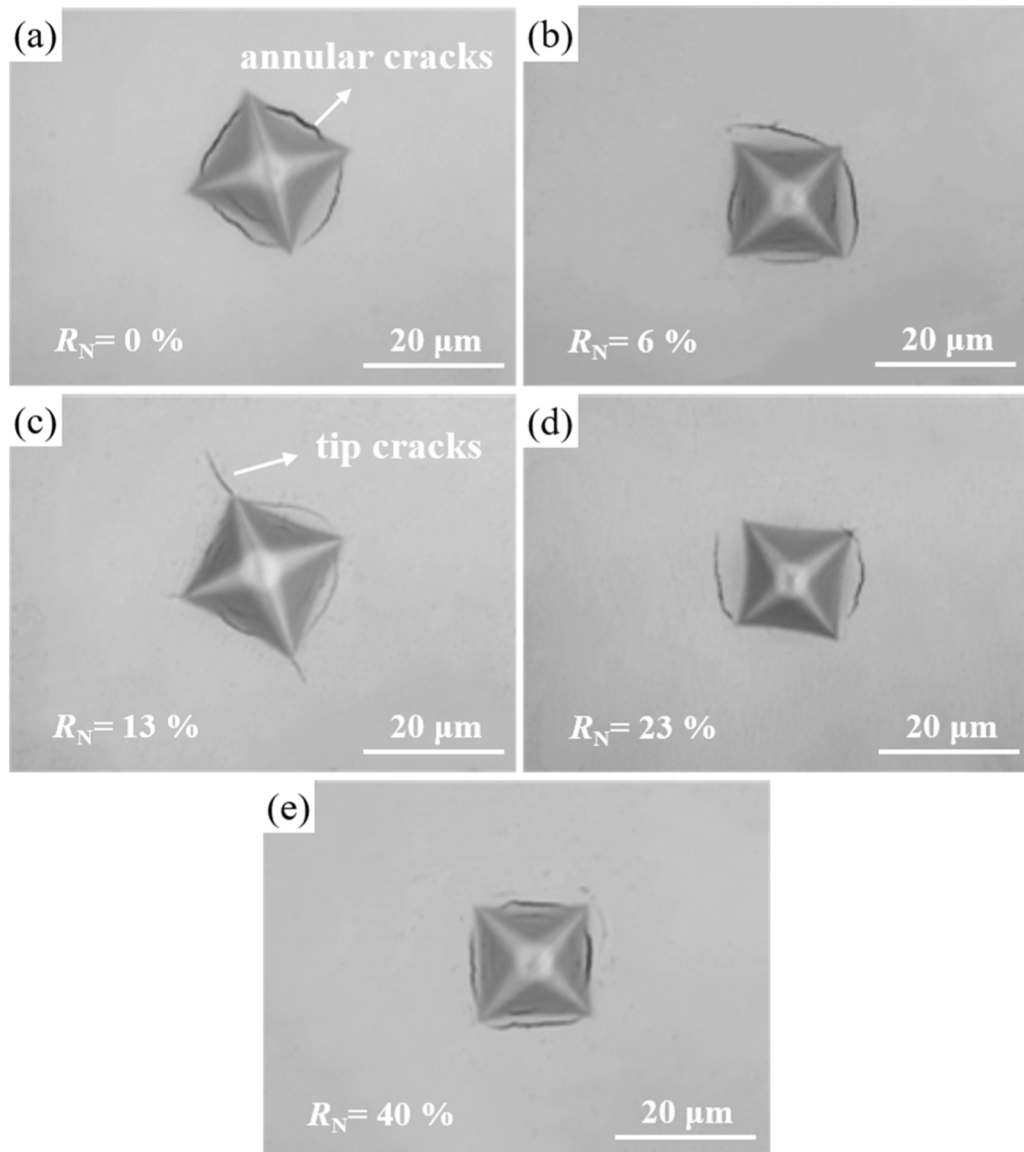


Fig. 9. Indentation morphology of $(Al_{0.5}CoCrFeNi)N_x$ films deposited at different R_N : (a) $R_N = 0\%$, (b) $R_N = 6\%$, (c) $R_N = 13\%$, (d) $R_N = 23\%$, (e) $R_N = 40\%$.

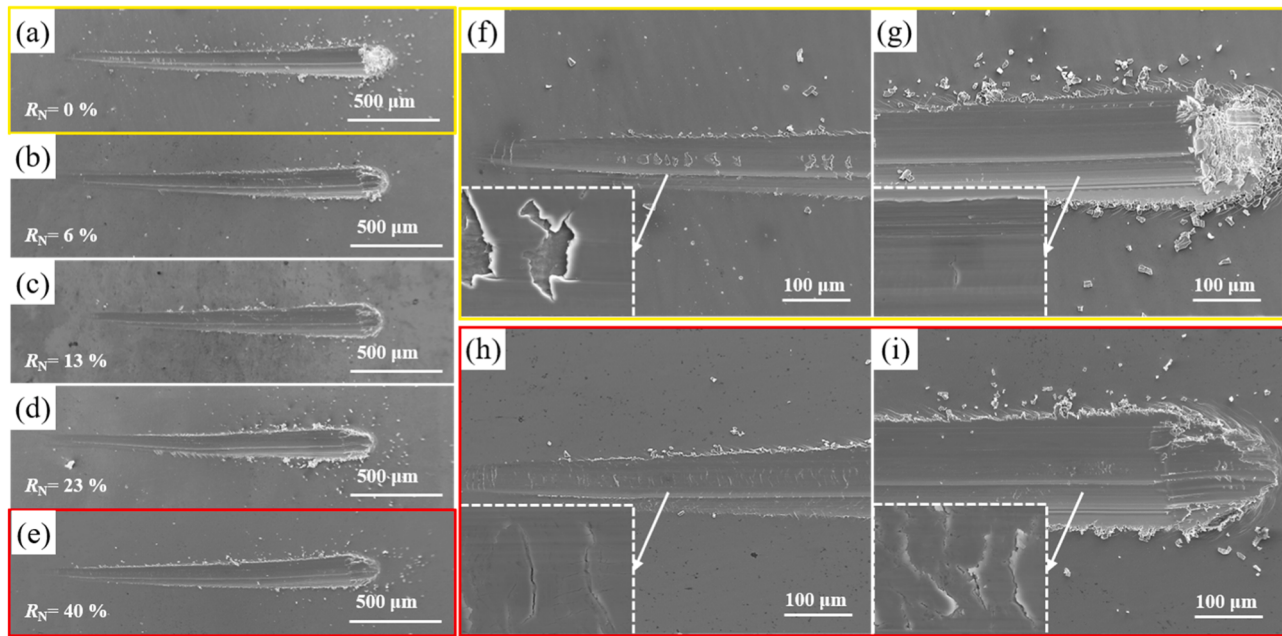


Fig. 10. Scratch morphology of $(\text{Al}_{0.5}\text{CoCrFeNi})_{\text{N}_x}$ films deposited at different R_{N} : (a) $R_{\text{N}} = 0\%$, (b) $R_{\text{N}} = 6\%$, (c) $R_{\text{N}} = 13\%$, (d) $R_{\text{N}} = 23\%$, (e) $R_{\text{N}} = 40\%$, (f-g) $R_{\text{N}} = 0\%$ mid-scratch and end-scratch, (h-i) $R_{\text{N}} = 40\%$ mid-scratch and end-scratch.

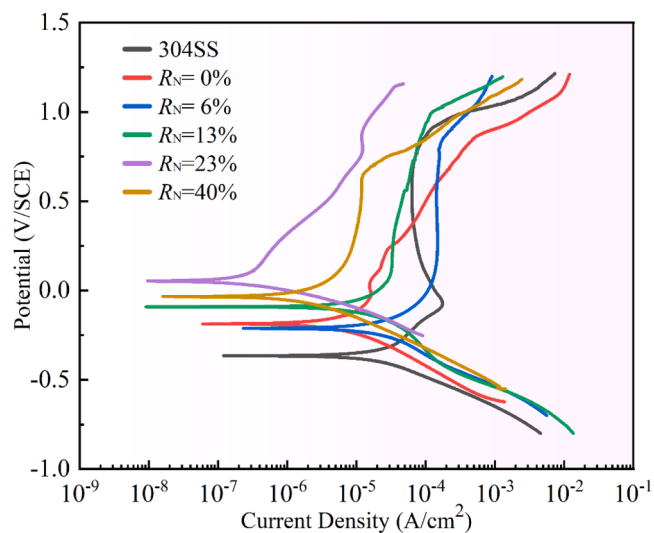


Fig. 11. Potentiodynamic polarization curves of 304SS and $(\text{Al}_{0.5}\text{CoCrFeNi})_{\text{N}_x}$ films deposited at different R_{N} in 3.5 wt% NaCl solution at room temperature.

Table 3
Electrochemical parameters of 304SS and $(\text{Al}_{0.5}\text{CoCrFeNi})_{\text{N}_x}$ films in 3.5 wt% NaCl solution.

Samples	E_{corr} (V/SCE)	I_{corr} ($\mu\text{A}/\text{cm}^2$)	β_a (V/dec)	$-\beta_b$ (V/dec)	R_p ($\Omega \text{ cm}^2$)
304SS	-0.365	18.47	0.308	0.151	2.09×10^4
$R_{\text{N}} = 0\%$	-0.186	6.98	0.279	0.150	5.32×10^4
$R_{\text{N}} = 6\%$	-0.211	15.19	0.209	0.189	3.27×10^4
$R_{\text{N}} = 13\%$	-0.087	6.52	0.277	0.182	6.51×10^4
$R_{\text{N}} = 23\%$	0.054	0.72	0.424	0.094	1.61×10^5
$R_{\text{N}} = 40\%$	-0.034	2.84	0.241	0.130	8.12×10^4

(7.7 mN). Notably, the load at $R_{\text{N}} = 13\%$ is only 6.8 mN. This is attributed to the fact that at $R_{\text{N}} = 13\%$, the crystalline structure of the HEAN films starts to undergo a transition from mainly FCC crystal structure to a mixed constitution of amorphous and nanocrystals. Fig. 8b gives the hardness and elastic modulus of HEAN films at different R_{N} . The $\text{Al}_{0.5}\text{CoCrFeNi}$ metallic film shows hardness and modulus of 11.63 GPa and 175.7 GPa, respectively. These values increase to 13.07 GPa and 210.6 GPa for HEAN film at $R_{\text{N}} = 6\%$, indicating the solution strengthen of nitrogen. The maximum hardness and modulus are observed at $R_{\text{N}} = 23\%$ (14.42 GPa and 212 GPa), much higher than the $\text{Al}_{0.5}\text{CoCrFeNi}$ film (11.63 GPa and 175.7 GPa). With further increase in R_{N} , the hardness and modulus decreased to 12.99 GPa and 194.1 GPa ($R_{\text{N}} = 40\%$).

In our previous studies [33,34], we referred to the ratio of the work of plastic deformation (W_p) to the total work of deformation (W_t) as the plasticity factor η_p ($\eta_p = W_p/W_t$), which was used to measure the plastic deformation ability of films. Moreover, the H/E ratio is used to assess the elastic strain-to-failure ability, while the H^3/E^2 ratio for plastic deformation resistance [35]. Table 2 lists the calculated η_p , H/E and H^3/E^2 values. All the deposited film shows high η_p ratio above 0.60, indicating good plastic deformation ability. However, Obviously, the HEAN film at $R_{\text{N}} = 23\%$ shows highest H^3/E^2 (0.067) and H/E ratio (0.068) with relative high η_p ratio (0.62), indicating superior toughness.

Actually, the as-deposited $\text{Al}_{0.5}\text{CoCrFeNi}$ film shows much higher hardness (11.63 GPa) than the melted $\text{Al}_{0.5}\text{CoCrFeNi}$ HEA (<5 GPa, [23, 25]). This is mainly attributed to the refinement of grains. With the addition of N atoms ($R_{\text{N}} = 6\%$), the further refinement of grains and solid solution of N in HEA lattice contribute to the hardness increase. However, at $R_{\text{N}} = 13\%$, the amorphous structure become apparent in the HEAN film, thus leading to the hardness decrease. As described in TEM (Fig. 7), the HEAN film at $R_{\text{N}} = 23\%$ show a structure of amorphous embedding nanocrystals, thus leading to a significant increase in hardness. With further increasing R_{N} , more N atoms are incorporated into the interstitial sites, inducing a reduction in the grain size (Fig. 4) and an increase in lattice distortion. In addition, the continuous bombardment of ions during sputtering makes the film structure denser (Fig. 3). Solid solution strengthening, fine grain strengthening and dense structure synergistically enhanced the properties of the films, contributing to the highest hardness at $R_{\text{N}} = 23\%$. However, increasing the R_{N} to 40%

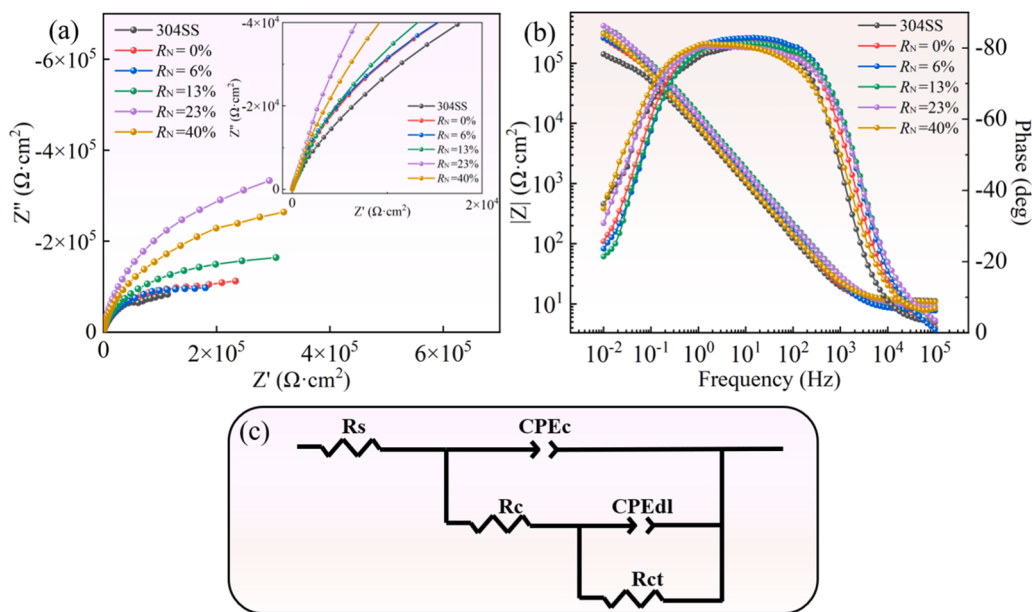


Fig. 12. Nyquist plots (a), Bode plots (b) and (c) Equivalent electrical circuit of 304SS and $(\text{Al}_{0.5}\text{CoCrFeNi})\text{N}_x$ films deposited at different R_N in 3.5 wt% NaCl solution at room temperature.

Table 4

Electrical equivalent circuit parameters of 304SS and $(\text{Al}_{0.5}\text{CoCrFeNi})\text{N}_x$ films in 3.5 wt% NaCl Solution.

Samples	R_s ($\Omega \cdot \text{cm}^2$)	CPE_c ($\text{S}^{*}\text{s}^{\alpha}$)	n	R_c ($\Omega \cdot \text{cm}^2$)	CPE_{ct} ($\text{S}^{*}\text{s}^{\beta}$)	m	R_{ct} ($\Omega \cdot \text{cm}^2$)
304SS	11.43	2.21×10^{-5}	0.921	9.62×10^3	1.16×10^{-4}	0.895	3.62×10^4
$R_N = 0\%$	8.75	1.87×10^{-5}	0.916	2.17×10^5	3.27×10^{-4}	1.313	4.27×10^4
$R_N = 6\%$	7.88	1.52×10^{-5}	0.927	1.95×10^5	1.88×10^{-4}	1.185	3.47×10^4
$R_N = 13\%$	9.48	1.31×10^{-5}	0.911	2.64×10^5	7.07×10^{-4}	1.705	3.17×10^4
$R_N = 23\%$	9.54	1.51×10^{-5}	0.897	4.39×10^5	8.61×10^{-4}	1.566	3.03×10^4
$R_N = 40\%$	11.28	2.17×10^{-5}	0.898	3.57×10^5	8.79×10^{-4}	1.538	2.25×10^4

causes an excess of N element, leading to the formation of nitride on the target surface due to target poisoning. As a result, a portion of the reactive sputtering of the film is converted into direct sputtering of the nitrides on the target surface during the sputtering process. This conversion not only leads to a decrease in the deposition rate of the film (Fig. 1a), but also leading to a slight decrease in mechanical properties. Similar results were reported in the research of Cui et al. [36].

The fracture toughness could be evaluated by indentation test [37–39]. Fig. 9 shows the indent morphology of $(\text{Al}_{0.5}\text{CoCrFeNi})\text{N}_x$ films under Vickers indentation. No obvious crack is observed inside the indentation, while cracks are visible around or at the tips of indentations. As seen from Fig. 9a-b, d-e, annular cracks occur around the indentations of films at $R_N = 0\%$, 6%, 23% and 40%, indicating acceptable toughness. The HEAN film at $R_N = 13\%$ shows obvious tip cracks (Fig. 9c), indicating poor fracture toughness, which is consistent with its low H/E ratio. The annular cracks occur before the high critical stress required for radial fracture is reached, and their presence may impede the appearance of radial cracks at the indentation tip, displaying better fracture toughness. By comparing the size of the annular crack, the highest fracture toughness occurs at $R_N = 23\%$. Actually, the indentation could reflect the mechanical properties of the films to a certain extent, which corresponds to the data measured by nanoindentation.

3.5. Scratch behavior of HEAN films

The morphology of the films after scratch test is presented in Fig. 10. As seen from Fig. 10a-e, all films exhibit excellent adhesion, with the scratch width increasing as the load rises. Throughout the load

application, no cracks appear on either side of the scratch, and the films dose not fail entirely due to good cohesion. At $R_N = 0\%$, a minor initial surface breakage occurs on the scratch surface due to the compressive effect of the sliding indenter on the front film (Fig. 10f). This creates a crack source that propagates within the film, causing failure of film cohesion. However, the interface crack does not significantly propagate with further indenter action. Generally, as the indenter slides and the load increases, the flexural height in the film rises, promoting the development and expansion of cracks at maximum tensile stress and film defects, ultimately leading to film fracture and surface breakage [40, 41].

Notably, despite increasing loads, a strong film/substrate bond prevents peeling. The scratch morphology remains consistent across different R_N (6–40%), and $R_N = 40\%$ is selected for detailed examination. The dissolution of N enhances the mechanical properties of the films and improves scratch resistance. In the initial stage of scratching (Fig. 10h), no surface breakage occurs. Instead, a small amount of tensile crack formation is generated due to the tangential friction between the indenter and the film. Initially, the stress effect of indenter on the film/base system is minimal, resulting in slight deformation. Film fracture predominantly occurs through direct fracture along the thickness of the film, with the fracture crack expanding at an angle relative to the scratch boundary and extending to the end of the scratch [42].

3.6. Electrochemical analysis of HEAN films

Fig. 11 displays the potentiodynamic curves of 304 stainless steel (304SS) and HEAN films at 3.5 wt% NaCl solution at room temperature. Table 3 summarizes the electrochemical parameters such as corrosion

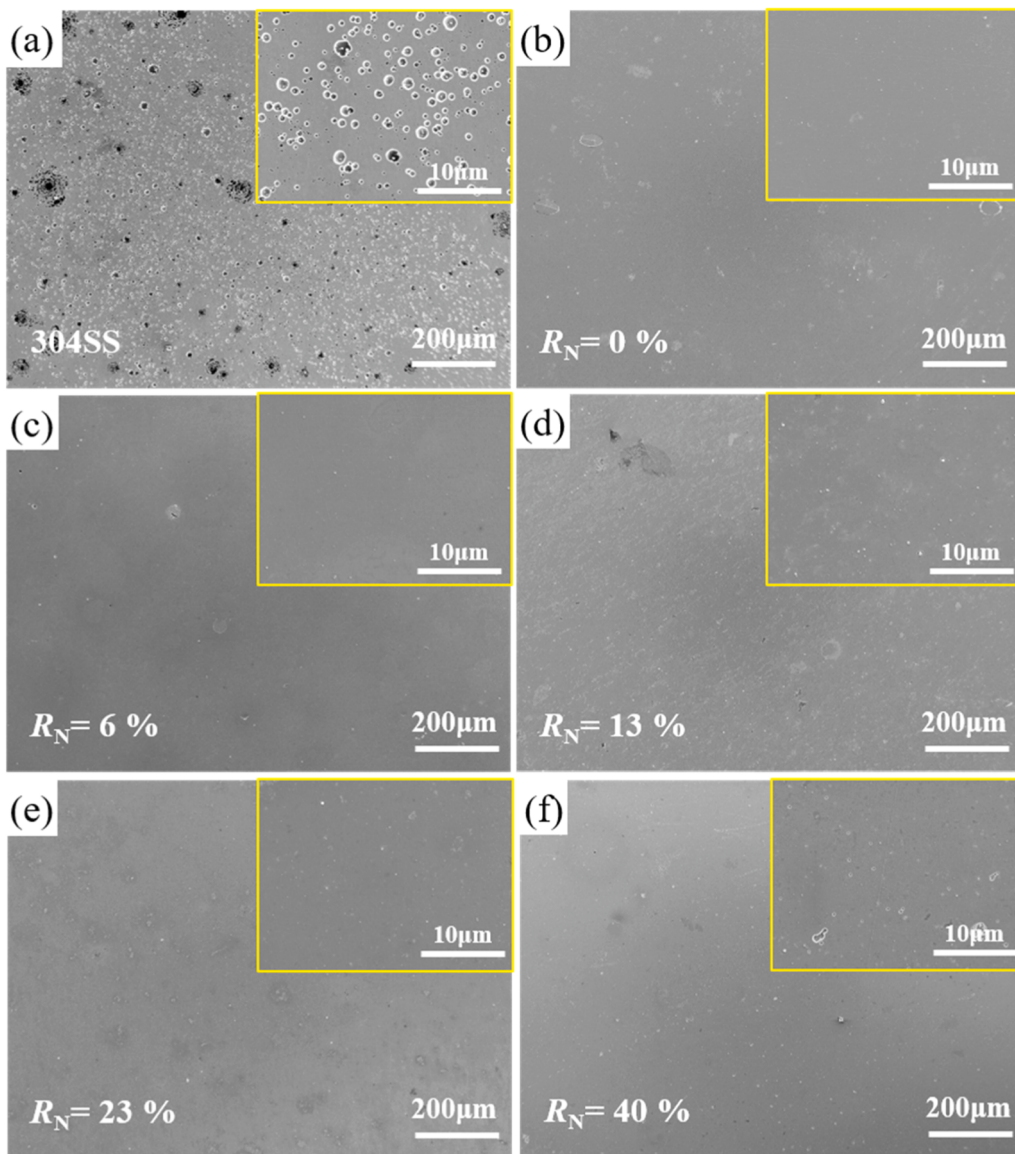


Fig. 13. Surface morphology of 304SS and $(\text{Al}_{0.5}\text{CoCrFeNi})\text{N}_x$ films deposited at different R_N after polarization test: (a) 304SS, (b) $R_N = 0\%$, (c) $R_N = 6\%$, (d) $R_N = 13\%$, (e) $R_N = 23\%$, (f) $R_N = 40\%$.

potential (E_{corr}), corrosion current density (I_{corr}), slope of the polarization curves (β_a , $-\beta_c$), and polarization resistance (R_p). Generally, better corrosion resistance is indicated by higher potentials and lower current densities [43]. The deposited HEAN films exhibit high potentials and low current densities density compared to 304SS. As shown in Table 3, the corrosion potential rises from -0.365 V (304SS) to 0.054 V ($R_N = 23\%$), while the corrosion current density decreased from $18.47\text{ }\mu\text{A}/\text{cm}^2$ to $0.72\text{ }\mu\text{A}/\text{cm}^2$. With increasing R_N ($>13\%$), the films form a uniform amorphous phase with lower defect concentration and higher chemical homogeneity, which slows down the diffusion of chloride ions and thus enhancing the corrosion resistance of the films [44]. Additionally, the film with $R_N = 23\%$ displayed no significant pitting potential observed in the scan range and showed significant resistance to chloride ion penetration and pitting. Therefore, the film with $R_N = 23\%$ demonstrates the best corrosion resistance.

The EIS results of 304SS and HEAN films are presented in Fig. 12. As seen from Fig. 12a, the Nyquist curves reveal that both the films and 304SS display similar capacitive arc at low frequencies and linear characteristics at high frequencies. Typically, a larger radius of the capacitance arc in the Nyquist curve implies a higher impedance and

better resistance to corrosion [45]. As reported by Zheng et al. [40], the amorphous with homogeneous microstructure and no localized heterogeneous defects would enhance the corrosion resistance. Notably, the HEAN films exhibit a significantly larger capacitive arc radius than 304SS, indicating enhanced corrosion resistance. In addition, at $R_N = 23\%$, the film is dominated by an amorphous structure exhibits the largest capacitive arc radius, suggesting the highest level of corrosion resistance.

Generally, the polarization resistance expressed in $|Z|_{0.01\text{ Hz}}$ is a useful measure of reaction corrosion resistance, with higher the $|Z|_{0.01\text{ Hz}}$ indicating better corrosion resistance [46]. As seen from Fig. 12b, the films exhibit an impedance of around 10^5 at 0.01 Hz and a maximum at $R_N = 23\%$. Due to the introduction of N, the crystal structure of the films transforms with increasing R_N towards an amorphous phase with excellent corrosion resistance. At high R_N , the amorphous structure becomes dominant. As a result, HEAN films possess higher corrosion resistance than the 304SS. Specifically, the films exhibit two time constants, one representing the bilayer effect of the film in the high-frequency range and the other signifying the bilayer effect of the film-substrate interface in the low-frequency range. At frequencies

between 10^4 - 10^5 Hz, the $|Z|$ values of both 304SS and films are approximately 10^1 . In the intermediate frequency range (10^1 - 10^3 Hz), the all Bode curves show a linear phase with a slope close to -1 . The relative phase angle approximates the largest value of the characteristic response reflecting the capacitive response and the $|Z|$ values for 304SS and films significantly converge in this intermediate range.

The electrical equivalent circuit (EEC) model shown in Fig. 12c was drawn according to the Fig. 12a-b, and Table 4 summarizes the results of the fit with Zview software. In the EEC model, the solution resistance is represented by R_s , and the resistance and capacitance caused by defects are represented by R_c and CPE_c . The charge transfer resistance and capacitance at the interface between the film and the substrate correspond to R_{ct} and CPE_{ct} . The quality of the film, which determines the corrosion resistance, is characterized by the polarization resistance (R_p). The values acquired from the fit were consistent with those of the Nyquist and Bode plots. As R_N increases, R_p improves from $9.62 \times 10^3 \Omega \text{ cm}^2$ (304SS) to $4.39 \times 10^5 \Omega \text{ cm}^2$ ($R_N = 23\%$), indicating that the deposited films exhibited a lower corrosion rate and stronger protection in NaCl solution. The corrosion-resistant elements such as Al and Cr in the films facilitate the formation of a dense oxide film. Also, the film shifts to an amorphous structure with increasing R_N , leading to an increase in charge transfer resistance [47]. Meanwhile, the higher R_N contribute to a more compact structure (Fig. 6), reducing flaws in the film [48]. This hinders the intrusion of corrosive media and enhances the corrosion resistance of the film.

Fig. 13 shows the surface morphology of 304SS and HEAN films after corrosion, and the corresponding enlarged images (marked in yellow) are shown at the top of each image. A considerable number of dense pits were observed on the surface of the 304SS (Fig. 13a). Conversely, the surface of the $(Al_{0.5}CoCrFeNi)_N_x$ HEAN films (Fig. 13b-f) exhibited no discernible damage and maintained a smooth and compact appearance. This observation confirms the exceptional corrosion resistance of the deposited HEAN films. The superior corrosion resistance of the $(Al_{0.5}CoCrFeNi)_N_x$ HEAN films can be primarily attributed to two factors. Firstly, these films contain a higher proportion of corrosion-resistant elements with robust passivation capabilities, facilitating the formation of densely layered oxide films. Secondly, by increasing the R_N , a large number of homogeneous amorphous phases with a disordered atomic arrangement are formed in the films, reducing the likelihood of heterogeneous defects and consequently enhancing the corrosion resistance.

4. Conclusion

In this study, $(Al_{0.5}CoCrFeNi)_N_x$ HEAN films with different N content were fabricated through reactive DC magnetron sputtering. The microstructure, mechanical and corrosion properties were investigated. The below conclusions could be drawn.

- (1) The deposition rate of the $(Al_{0.5}CoCrFeNi)_N_x$ HEAN films decreased from 18.53 nm/min to 10.15 nm/min as the R_N increased. Additionally, the nitrogen content in the films showed an upward trend, reaching 33 at\% at the highest R_N . The HEAN film exhibited a biphasic hybrid structure comprising of FCC and BCC phases at $R_N = 0\%$. The crystallinity of the $(Al_{0.5}CoCrFeNi)_N_x$ films decreased with increasing nitrogen content. The structure transformed from a composite phase of FCC and BCC ($R_N = 0\%$) to a mixture phase of FCC nanocrystalline and amorphous phase ($R_N > 13\%$).
- (2) With the increase of R_N , the hardness and modulus of the films changed from 11.63 GPa and 175.7 GPa ($R_N = 0\%$) to 14.42 GPa and 212 GPa ($R_N = 23\%$), respectively. Fracture toughness demonstrated a similar trend to the hardness. Scratch tests indicated favorable toughness of the films and excellent adhesion to the substrate.

- (3) The HEAN films showed increased potential and lower current density compared to 304SS, with the highest durability at $R_N = 23\%$. The dissolution of nitrogen facilitates the films transition to amorphous, which reduced the corrosion micro-pores and enhanced the corrosion resistance.

CRediT authorship contribution statement

Fanyong Zhang: Conceptualization, Methodology, Writing – original draft. **Honglu Ma:** Data curation, Writing – original draft preparation. **Ruixin Zhao:** Data curation. **Guangxing Yu:** Data curation. **Jiawen Chen:** Data curation. **Fuxing Yin:** Reviewing.

Declaration of Competing Interest

The authors declare that they have no known competing financial interests or personal relationships that could have appeared to influence the work reported in this paper.

Data Availability

No data was used for the research described in the article.

Acknowledgements

The authors gratefully acknowledge Natural Science Foundation of Hebei province (Grant No. E2020202110) and National Natural Science Foundation of China (Grant No. 51701062) for the financial support of this research work.

References

- [1] J.W. Yeh, S.K. Chen, S.J. Lin, et al., Nanostructured high-entropy alloys with multiple principal elements: novel alloy design concepts and outcomes, *Adv. Eng. Mater.* 6 (2004) 299–303.
- [2] Y.P. Lu, X.Z. Gao, L. Jiang, et al., Directly cast bulk eutectic and near-eutectic high entropy alloys with balanced strength and ductility in a wide temperature range, *Acta Mater.* 124 (2017) 143–150.
- [3] D. Ma, B. Grabowski, F. Körmann, et al., Ab initio thermodynamics of the CoCrFeMnNi high entropy alloy: Importance of entropy contributions beyond the configurational one, *Acta Mater.* 100 (2015) 90–97.
- [4] K.Y. Tsai, M.H. Tsai, J.W. Yeh, Sluggish diffusion in Co–Cr–Fe–Mn–Ni high-entropy alloys, *Acta Mater.* 61 (2013) 4887–4897.
- [5] B. Gludovatz, A. Hohenwarter, D. Catoor, et al., A fracture-resistant high-entropy alloy for cryogenic applications, *Science* 345 (2014) 1153–1158.
- [6] C. Lee, G. Song, M.C. Gao, et al., Lattice distortion in a strong and ductile refractory high-entropy alloy, *Acta Mater.* 160 (2018) 158–172.
- [7] D. Chung, Z. Ding, Y. Yang, Hierarchical eutectic structure enabling superior fracture toughness and superb strength in CoCrFeNiNb_{0.5} eutectic high entropy alloy at room temperature, *Adv. Eng. Mater.* 21 (2018).
- [8] J. Li, Y. Huang, X. Meng, et al., A review on high entropy alloys coatings: fabrication processes and property assessment, *Adv. Eng. Mater.* 21 (2019), 1900343.
- [9] X.H. Yan, J.S. Li, W.R. Zhang, et al., Physics, a brief review of high-entropy films, *Mater. Chem.* 210 (2018) 12–19.
- [10] W. Li, P. Liu, P.K. Liaw, Microstructures and properties of high-entropy alloy films and coatings: a review, *Mater. Res. Lett.* 6 (2018) 199–229.
- [11] J. Guo, Z.B. Cai, Y.J. Guan, et al., High temperature wear performance of laser-cladded FeNiCoAlCu high-entropy alloy coating, *Appl. Surf. Sci.* 445 (2018) 113–122.
- [12] Z.B. Cai, Y.D. Wang, X.F. Cui, et al., Design and microstructure characterization of FeCoNiAlCu high-entropy alloy coating by plasma cladding: in comparison with thermodynamic calculation, *Surf. Coat. Technol.* 330 (2017) 163–169.
- [13] X. Lu, C. Zhang, X. Zhang, et al., Dependence of mechanical and tribological performance on the microstructure of (CrAlTiNbVN)_x high-entropy nitride coatings in aviation lubricant, *Ceram. Int.* 47 (2021) 27342–27350.
- [14] Y. Wang, Y. Yang, H. Yang, et al., Microstructure and wear properties of nitrided AlCoCrFeNi high-entropy alloy, *Mater. Chem. Phys.* 210 (2018) 233–239.
- [15] W. Xu, M. Liao, X. Liu, et al., Microstructures and properties of (TiCrZrVAl)_N high entropy ceramics films by multi-arc ion plating, *Ceram. Int.* 47 (2021) 24752–24759.
- [16] D. Depla, R. Dedoncker, K. Strijckmans, Nitride formation during reactive sputter deposition of multi-principal element alloys in argon/nitrogen mixtures, *Thin Solid Films* 732 (2021), 138721.

- [17] L. Chen, W. Li, P. Liu, et al., Microstructure and mechanical properties of $(\text{AlCrTiZrV})_N$ high-entropy alloy nitride films by reactive magnetron sputtering, *Vacuum* 181 (2020), 109706.
- [18] N.A. Khan, B. Akhavan, C. Zhou, et al., High entropy nitride (HEN) thin films of $\text{AlCoCrCu}_{0.5}\text{FeNi}$ deposited by reactive magnetron sputtering, *Surf. Coat. Technol.* 402 (2020), 126327.
- [19] M.E. Garah, D.E. Touaibia, S. Achache, et al., Effect of nitrogen content on structural and mechanical properties of $\text{AlTiZrTaHf}(N)$ high entropy films deposited by reactive magnetron sputtering, *Surf. Coat. Technol.* 432 (2022), 128051.
- [20] C. Zhang, X. Lu, C. Wang, et al., Tailoring the microstructure, mechanical and tribocorrosion performance of $(\text{CrNbTiAlV})_N$ high-entropy nitride films by controlling nitrogen flow, *J. Mater. Sci. Technol.* 107 (2022) 172–182.
- [21] R. Chen, Z. Cai, J. Pu, et al., Effects of nitriding on the microstructure and properties of VALiCrMo high-entropy alloy coatings by sputtering technique, *J. Alloy. Compd.* 827 (2020), 153836.
- [22] Y. Si, G. Wang, M. Wen, et al., Corrosion and friction resistance of TiCrZrWN_x high entropy ceramics coatings prepared by magnetron sputtering, *Ceram. Int.* 48 (2022) 9342–9352.
- [23] C.M. Lin, H.L. Tsai, Evolution of microstructure, hardness, and corrosion properties of high-entropy $\text{Al}_{0.5}\text{CoCrFeNi}$ alloy, *Intermetallics* 19 (2011) 288–294.
- [24] Y. Shi, L. Collins, N. Balke, et al., In-situ electrochemical-AFM study of localized corrosion of $\text{Al}_x\text{CoCrFeNi}$ high-entropy alloys in chloride solution, *Appl. Surf. Sci.* 439 (2018) 533–544.
- [25] M. Izadi, M. Soltanieh, S. Almalhoda, et al., Microstructural characterization and corrosion behavior of $\text{Al}_x\text{CoCrFeNi}$ high entropy alloys, *Mater. Chem. Phys.* 273 (2021), 124937.
- [26] B. Ren, R. Zhao, G. Zhang, et al., Microstructure and properties of the $\text{AlCrMoZrTi}/(\text{AlCrMoZrTi})\text{N}$ multilayer high-entropy nitride ceramics films deposited by reactive RF sputtering, *Ceram. Int.* 48 (2022) 16901–16911.
- [27] B.S. Lou, C.J. Wang, Y.Y. Chen, et al., Phase, mechanical property and corrosion resistance evaluation of W-Nb-Ta-Ti and W-Nb-Ta-Ti-N medium entropy alloy thin films, *Surf. Coat. Technol.* 442 (2022), 128339.
- [28] S.A. Kube, S. Sohn, D. Uhl, et al., Phase selection motifs in High Entropy Alloys revealed through combinatorial methods: Large atomic size difference favors BCC over FCC, *Acta Mater.* 166 (2019) 677–686.
- [29] W.R. Wang, W.L. Wang, S.C. Wang, et al., Effects of Al addition on the microstructure and mechanical property of $\text{Al}_x\text{CoCrFeNi}$ high-entropy alloys, *Intermetallics* 26 (2012) 44–51.
- [30] T.K. Chen, T.T. Shun, J.W. Yeh, et al., Nanostructured nitride films of multi-element high-entropy alloys by reactive DC sputtering, *Surf. Coat. Technol.* 188–189 (2012) 193–200.
- [31] H.T. Hsueh, W.J. Shen, M.H. Tsai, et al., Effect of nitrogen content and substrate bias on mechanical and corrosion properties of high-entropy films $(\text{AlCrSiTiZr})_{100-x}\text{N}_x$, *Surf. Coat. Technol.* 206 (2012) 4106–4112.
- [32] L.L. Xiao, Z.Q. Zheng, S.W. Guo, et al., Ultra-strong nanostructured CrMnFeCoNi high entropy alloys, *Mater. Des.* 194 (2020), 108895.
- [33] F. Zhang, Y. Ding, S. Yan, et al., Microstructure evolution and mechanical performance of Cr-N/Al-Cr multilayer coatings produced by plasma nitriding Cr-coated Al alloy, *Vacuum* 180 (2020), 109540.
- [34] L. Wang, F. Zhang, S. Yan, et al., Microstructure evolution and mechanical properties of atmosphere plasma sprayed AlCoCrFeNi high-entropy alloy coatings under post-annealing, *J. Alloy. Compd.* 872 (2021), 159607.
- [35] A. Leyland, A. Matthews, On the significance of the H/E ratio in wear control: a nanocomposite coating approach to optimised tribological behaviour, *Wear* 246 (2000) 1–11.
- [36] P. Cui, W. Li, P. Liu, et al., Effects of nitrogen content on microstructures and mechanical properties of $(\text{AlCrTiZrHf})\text{N}$ high-entropy alloy nitride films, *J. Alloy. Compd.* 834 (2020), 155063.
- [37] A.A. Volinsky, N.R. Moody, W.W. Gerberich, Interfacial toughness measurements for thin films on substrates, *Acta Mater.* 50 (2002) 441–466.
- [38] W. Li, T. Siegmund, An analysis of the indentation test to determine the interface toughness in a weakly bonded thin film coating – substrate system, *Acta Mater.* 50 (2004) 2989–2999.
- [39] M. Zhao, X. Chen, Y. Xiang, et al., Measuring elastoplastic properties of thin films on an elastic substrate using sharp indentation, *Acta Mater.* 55 (2007) 6260–6274.
- [40] M. Zawischa, M. Supian, S. Makowski, et al., Generalized approach of scratch adhesion testing and failure classification for hard coatings using the concept of relative area of delamination and properly scaled indenters, *Surf. Coat. Technol.* 415 (2021), 127118.
- [41] X. Jin, C. Hou, Y. Zhao, et al., Mechanical properties and deformation mechanisms of $(\text{Ti}_{0.2}\text{Zr}_{0.2}\text{Nb}_{0.2}\text{Hf}_{0.2})\text{C}$ high-entropy ceramics characterized by nanoindentation and scratch tests, *Ceram. Int.* 48 (2022) 35445–35451.
- [42] S. Kataria, N. Kumar, S. Dash, et al., Evolution of deformation and friction during multimode scratch test on TiN coated D9 steel, *Surf. Coat. Technol.* 205 (2010) 922–927.
- [43] S. Zheng, Z. Cai, J. Pu, et al., A feasible method for the fabrication of VALiCrSi amorphous high entropy alloy film with outstanding anti-corrosion property, *Appl. Surf. Sci.* 483 (2019) 870–874.
- [44] S. Zheng, Z. Cai, J. Pu, et al., Passivation behavior of VALiCrSi amorphous high-entropy alloy film with a high corrosion-resistance in artificial sea water, *Appl. Surf. Sci.* 542 (2021), 148520.
- [45] P. Wu, K. Gan, D. Yan, et al., A non-equiautomic FeNiCoCr high-entropy alloy with excellent anti-corrosion performance and strength-ductility synergy, *Corros. Sci.* 183 (2021), 109341.
- [46] K. Yu, W. Zhao, Z. Li, et al., High-temperature oxidation behavior and corrosion resistance of in-situ TiC and Mo reinforced AlCoCrFeNi -based high entropy alloy coatings by laser cladding, *Ceram. Int.* 49 (2023) 10151–10164.
- [47] W. Muffah, J. Allport, V. Vishnyakov, Corrosion performance and mechanical properties of FeCrSiNb amorphous equiatomic HEA thin film, *Surf. Coat. Technol.* 422 (2021), 127486.
- [48] C. Zhang, X. Lu, H. Zhou, et al., Construction of a compact nanocrystal structure for $(\text{CrNbTiAlV})_N$ high-entropy nitride films to improve the tribo-corrosion performance, *Surf. Coat. Technol.* 429 (2022), 127921.